ACS NANO

www.acsnano.org

Topology-Driven Sodium Storage and Conversion in Covalent Fullerene Networks

Hao Mei,[⊥] Qiuchen Xu,[⊥] Shitao Wu, Yan Wang, Wentao Fan, Yuxuan Zhang, Shuo Wang, Hui Yu, Shitao Geng, Chengxiao Zhang, Shanshan Tang, Antonio Gaetano Ricciardulli, Yiyong Mai, Huisheng Peng, Hao Sun,* Paolo Samorì,* and Sheng Yang*

Cite This: https://doi.org/10.1021/acsnano.6c09620

Read Online

ACCESS | Metrics & More | Article Recommendations | Supporting Information

ABSTRACT: **Fullerene network is an emergent two-dimensional (2D) carbon allotrope in which C_{60} molecules are covalently bonded to form a quasi-hexagonal pattern (qHP). The intermolecular covalent bonding significantly reshapes the intrinsic electronic structure of the C_{60} units, leading to enhanced structural stability and electrochemical activity. Herein, we report unconventional high-density Na-ion storage and electrocatalytic conversion properties of fullerene networks (qHP-C_{60}) driven by their covalent quasi-hexagonal topology. As an anode material for sodium-ion batteries, the covalent framework facilitates intermolecular charge transfer and creates favorable sites for Na^+ adsorption, delivering a maximum reversible capacity of 279 mAh g^{-1} at 25 mA g^{-1}. In addition, the interconnected and curved C_{60} subunits induce inhomogeneous electron distribution, accelerating the reaction kinetics of $NaCl/Cl_2$ conversion in sodium-chlorine batteries. This enables a high current density (15,000 mA g^{-1} versus 1,000−1,500 mA g^{-1}) at a significantly reduced catalyst loading amount (5 wt % versus 60−80 wt %) compared to benchmark catalysts. Our study provides insights into the covalent structural engineering of carbon materials for high-performance energy applications.**

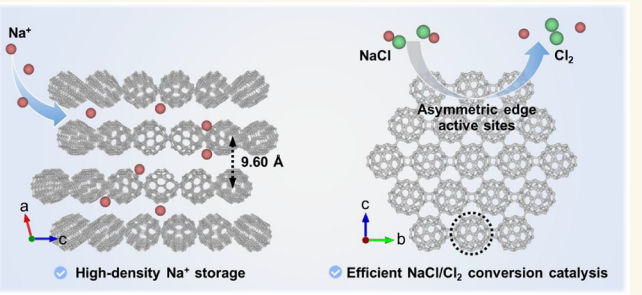

KEYWORDS: *fullerene network, carbon materials, sodium-chlorine batteries, sodium-ion batteries, carbon electrocatalyst*

INTRODUCTION

High-performance carbon materials are essential to various energy harvesting and storage technologies.[1−3] Among them, graphite has dominated the lithium-ion battery anode for decades owing to its structural stability and optimal electrochemical potential.[4,5] However, extending graphite to more sustainable and high-performance battery systems, such as intercalation-type sodium (Na)-ion batteries and conversion-type Na−S, Na−O_2, and Na−Cl_2 batteries, remains a major challenge. The narrow interlayer gap of graphite (3.35 Å) imposes a high energy barrier for Na-ion intercalation, yielding very low capacities of only 12−35 mAh g^{-1} in Na-ion batteries.[6] Moreover, the highly stable and symmetric hexagonal carbon lattice of graphite cannot provide sufficient active sites to catalyze the redox reactions in conversion-type batteries.[7,8] Although chemical modification strategies, such as heteroatom doping or disorder engineering, have been extensively explored to enhance Na-ion storage and electrocatalytic performance,[9−14] state-of-the-art carbon materials, such as heteroatom-doped carbon, porous graphite, and carbon nanotubes, still face a fundamental trade-off between these two functions within a single structure.[15,16] Thus, integrating high-capacity Na-ion storage and intrinsic catalytic activity into one carbon material is highly desirable, yet remains a significant challenge for advancing electrochemical performance.

From a structural perspective, carbon materials are typically constructed using carbon atoms as fundamental building units. Recently, carbon clusters have emerged as new building blocks for the topological engineering of crystalline carbon materials,[17−20] including long-range ordered porous carbon,[21] ultrahard amorphous carbon,[22] and polymerized phase of C_{60},[23] enabling numerous unique properties. For example, Hou et al. and Meirzadeh et al. prepared monolayer and few-layer polymeric C_{60} networks,[2,3] in which individual C_{60} clusters exhibit hexagonal coordination with six neighboring fullerene cages oriented along the equatorial plane, featuring interlinked bonding configurations that include both C−C connections

Received: May 22, 2026
Revised: August 3, 2026
Accepted: August 4, 2026

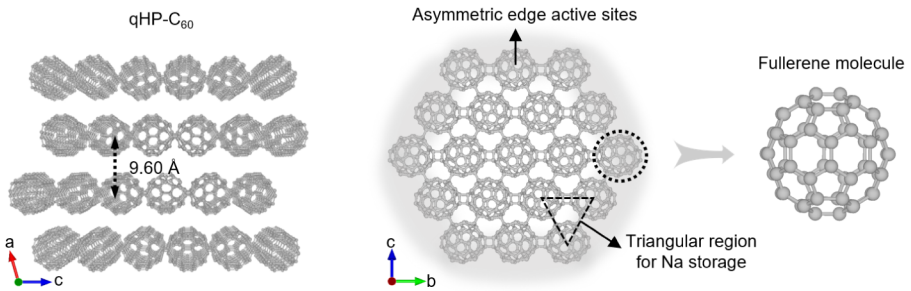

Figure 1. Schematic of the qHP-C_{60} framework based on covalently bonded C_{60} molecules. The interlayer gap of the layered qHP-C_{60} crystal is 9.60 Å.

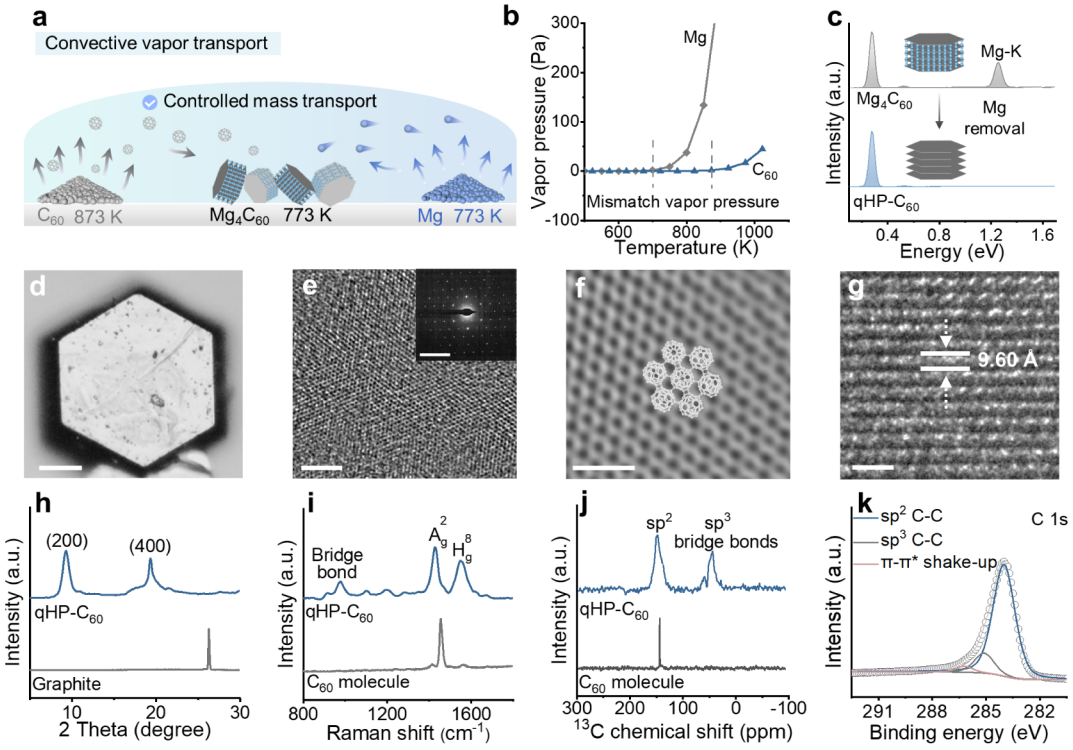

Figure 2. Synthesis and the characterizations of qHP-C_{60}. (a) Schematic illustration of the convective chemical vapor transport approach for the growth of Mg_4C_{60} crystal. (b) Temperature-dependent vapor pressures of Mg and C_{60}. (c) Energy-dispersive spectrometer test of Mg_4C_{60} and qHP-C_{60}. (d) Optical microscope image of a typical qHP-C_{60} crystal. The scale bar is 20 μm. (e) High-resolution TEM image of qHP-C_{60}. The scale bar is 5 nm. Inset: selected area electron diffraction pattern. The scale bar is 4 nm^{-1}. (f) Inverse fast Fourier-transformed high-resolution TEM image of qHP-C_{60}. The scale bar is 2 nm. (g) High-resolution TEM image of the cross-section of qHP-C_{60}. The measured interlayer gap of qHP-C_{60} is 9.60 Å. The scale bar is 2 nm. (h) XRD patterns of graphite and qHP-C_{60}. (i) Raman spectra of C_{60} molecules and qHP-C_{60}. (j) Magic-angle-spinning solid-state ^{13}C NMR spectra of C_{60} molecules and qHP-C_{60}. (k) C 1s XPS spectrum of qHP-C_{60}.

and [2 + 2] cycloaddition bridges. These pioneering works suggest that the rational design of C_{60} networks may offer new electrochemical properties of carbon materials toward advanced battery applications.

To address the structure−property trade-offs in many carbon materials, this study introduces a molecular engineering strategy for preparing layered qHP-C_{60}, enabling high-capacity Na-ion storage and efficient electrocatalytic $NaCl/Cl_2$ conversion. The scope of this work includes the scaled-up synthesis of qHP-C_{60} materials, Na-ion storage properties, and their catalytic performance in conversion-type $NaCl/Cl_2$ batteries (Figure 1). Especially, layered qHP-C_{60} exhibits a large interlayer spacing of 9.60 Å, providing spacious channels for rapid Na-ion intercalation and deintercalation. The covalent intermolecular bridge bonds generate a high density of accessible active sites that promote Na^+ adsorption and storage, providing a substantial Na-ion storage capacity of up to 279 mAh g^{-1} at 25 mA g^{-1}. The nonuniform electron density localized at the edges significantly enhances the catalytic activity toward $NaCl/Cl_2$ conversion, enabling a record rate capability of 15,000 mA g^{-1} while reducing the catalyst loading from 60−80 wt % to 5 wt %. Our results open a new avenue for high-performance energy storage by *de novo* molecular engineering of carbon materials.

RESULTS AND DISCUSSION

Scalable Synthesis of qHP-C_{60}

The synthesis of layered qHP-C_{60} in large quantities is essential for studying its electrochemical performance. The overall

https://doi.org/10.1021/acsnano.6c09620
ACS Nano XXXX, XXX, XXX−XXX

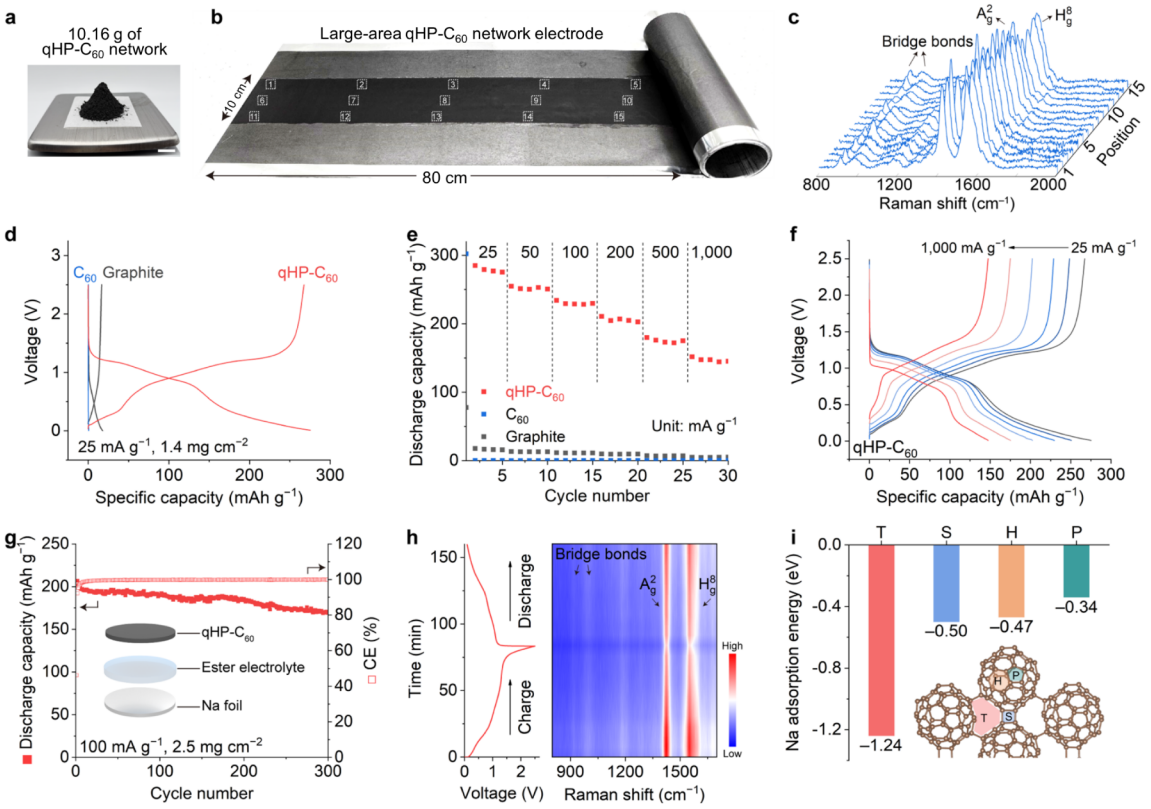

Figure 3. Electrochemical performance of qHP-C_{60} in Na-ion batteries. (a) Photograph of ~10 g qHP-C_{60} powder. The scale bar is 2 cm. (b) Photograph of a 0.8 × 0.1 m^2 qHP-C_{60} electrode. (c) Raman spectra of the corresponding 15 marked positions on the qHP-C_{60} electrode in (b). (d) Galvanostatic charge−discharge curves of Na||graphite, Na||C_{60}, and Na||qHP-C_{60} cells at a current density of 25 mA g^{-1}. (e) Rate performance of graphite, C_{60}, and qHP-C_{60}. (f) Galvanostatic charge−discharge curves of qHP-C_{60} at increasing current densities from 25 to 1,000 mA g^{-1}. The mass loadings of anode materials in d-f are 1.4 mg cm^{-2}. (g) Cycling performance of the Na||qHP-C_{60} cell at a current density of 100 mA g^{-1}. The mass loading of qHP-C_{60} is 2.5 mg cm^{-2}. (h) *In situ* Raman spectra of qHP-C_{60} during charge and discharge at the 2nd cycle with a current density of 100 mA g^{-1}. (i) Schematic illustration and the corresponding Na adsorption energies of potential Na adsorption sites in qHP-C_{60}. T, S, H, and P represent triangle, square, hexagon, and pentagon sites, respectively.

synthetic route of qHP-C_{60} involves two steps, including the growth of high-quality Mg_4C_{60} crystals and the subsequent selective Mg extraction (Figure S1 and Experimental Section). The Mg_4C_{60} precursor features in-plane covalent C_{60} networks stabilized by strong out-of-plane Mg−C interactions. We developed a customized convective chemical vapor transport process, wherein Mg and C_{60} sources were spatially separated into independently controlled temperature zones (T_1 = 773 K for Mg, T_2 = 873 K for C_{60}, respectively, Figure 2a). This design accommodates their different vapor pressures and enables scalable growth of high-quality Mg_4C_{60} crystals (Figures 2b and S2−S5). Subsequent topochemical removal of Mg^{2+} ions was achieved through a mild two-step etching protocol. Initial treatment with nitric acid weakened Mg−C interactions to release Mg^{2+} ions, followed by the addition of salicylic acid to provide a competitive coordination that ensured complete Mg^{2+} extraction, yielding phase-pure layered qHP-C_{60} (Figure 2c). Notably, the mild Mg removal process did not break the layered qHP-C_{60} crystals into single- or few-layer nanosheets, as confirmed by its low specific surface area of 4.04 m^2 g^{-1}, measured by N_2 adsorption−desorption isotherms (Figure S6).

The qHP-C_{60} exhibits well-defined hexagonal crystalline structures with an average particle size of ~100 μm, as validated by optical microscopy and SEM (Figures 2d, S7−S8). High-resolution transmission electron microscopy (HR-TEM) showed a honeycomb-like hexagonal pattern (Figure 2e). This was further validated by bandpass-filtered inverse fast Fourier transform (iFFT), which removed aperiodic pixel noise and highlighted the distinct hexagonal topology of the interlinked C_{60} subunits (Figure 2f). Cross-sectional HR-TEM imaging revealed an interlayer gap of 9.60 Å (Figure 2g), consistent with X-ray diffraction (XRD) analysis that displayed two characteristic diffraction peaks at 9.26° and 19.35°, corresponding to the (200) and (400) planes, respectively (Figure 2h). Spectroscopic analysis confirmed the transformation from molecular C_{60} to layered qHP-C_{60}. Raman spectra showed the characteristic qHP-C_{60} peaks at 1,426 cm^{-1} and 1,551 cm^{-1}, attributed to the pentagonal-pinch (A_g^2) and hexagon shear (H_g^8) vibrational modes, respectively (Figure 2i). The A_g^2 mode, which is highly sensitive to cage geometry and electron density redistribution, shifted to lower wavenumber, from 1,451 cm^{-1} in molecular C_{60} to 1,426 cm^{-1}, indicating C_{60} cage distortion induced by covalent bonding.[2] The intermolecular bonding reduces the symmetry of the C_{60} cage, giving rise to two new vibrational modes at 916 cm^{-1} and 975 cm^{-1}, which are associated with intermolecular sp^3-type bonds formed upon polymerization.[18,24−26] This is further supported by magic-angle-spinning solid-state ^{13}C nuclear magnetic resonance (NMR), which reveals two distinct emerging resonances at 59.9 and 44.1 ppm (Figure 2j).[27,28] In addition,

https://doi.org/10.1021/acsnano.6c09620
ACS Nano XXXX, XXX, XXX−XXX

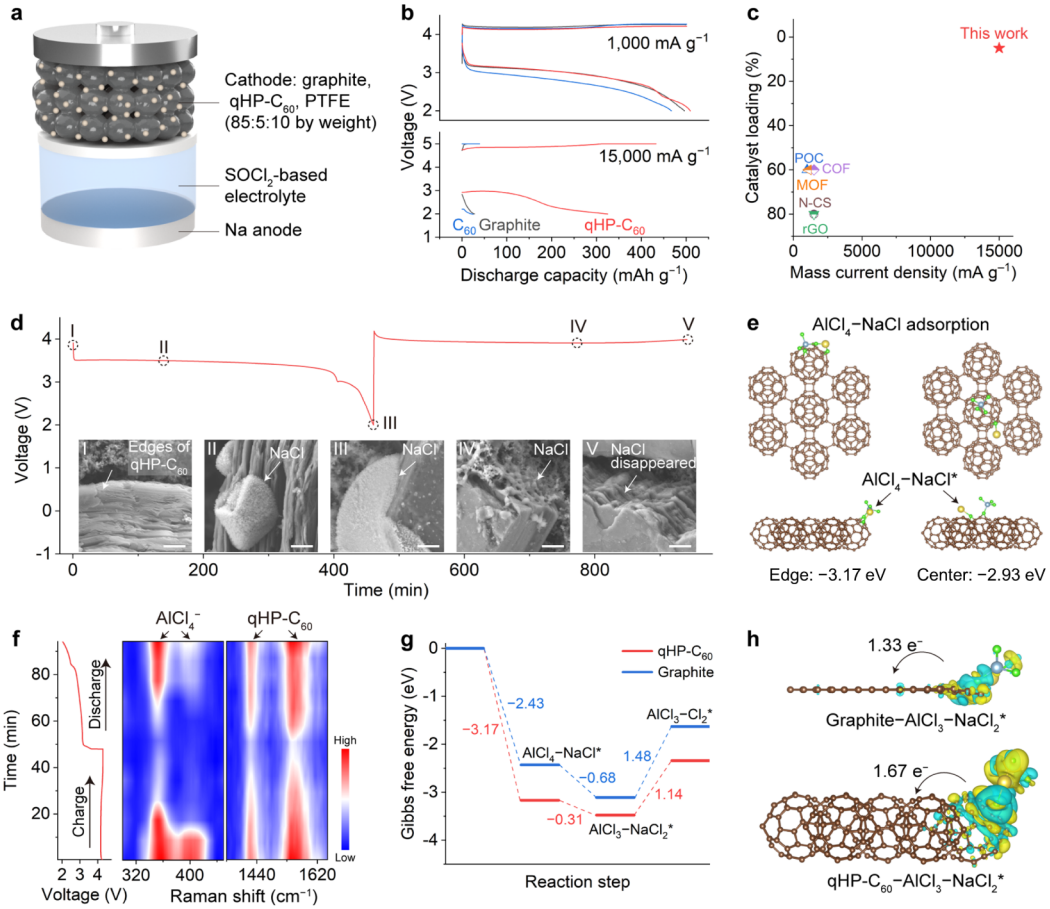

Figure 4. Electrochemical performance of qHP-C_{60} as high-performance cathode catalyst for rechargeable Na−Cl_2 battery. (a) Schematic illustration of a rechargeable Na−Cl_2 battery based on a cathode composed of graphite, qHP-C_{60}, and PTFE in a weight ratio of 85:5:10. (b) Galvanostatic charge−discharge curves of rechargeable Na−Cl_2 batteries based on bare graphite cathodes and graphite cathodes with 5 wt % qHP-C_{60} or 5 wt % C_{60}. The current densities are 1,000 mA g^{-1} and 15,000 mA g^{-1}. (c) Comparison of catalyst loading and maximum areal current based on various cathode catalysts in rechargeable Na−Cl_2 batteries, including metal−organic framework (MOF, UiO-66-NH_2),[34] covalent organic framework (COF-NH_2),[35] porous organic nanocage (POC),[36] reduced graphene oxide (rGO),[37] and nitrogen-doped carbon nanosheets (N-CS).[38] (d) SEM images of qHP-C_{60} cathodes from the rechargeable Na−Cl_2 batteries at various charge and discharge states. The current density and specific capacity are 500 mA g^{-1} and 500 mAh g^{-1}, respectively. The scale bars are 500 nm. (e) Optimized structures of $AlCl_4$−NaCl on the edge (left) and the center of qHP-C_{60} (right). (f) *In situ* Raman spectra of the electrolyte (300−450 cm^{-1}) and qHP-C_{60} (1,350−1,650 cm^{-1}) during continuous charge and discharge. The current density and specific capacity are 1,000 mA g^{-1} and 500 mAh g^{-1}, respectively. (g) Calculated Gibbs free energies of NaCl oxidation on the edge of graphite and qHP-C_{60}. (h) Differential charge density distributions of the adsorbed $AlCl_3$−$NaCl_2$* reaction intermediates on graphite (up) and qHP-C_{60} (down), respectively. The yellow and cyan areas represent the accumulation and depletion of electron densities, respectively.

the sp^2 carbon resonance shifted from 143.8 to 148.5 ppm due to covalent assembly of C_{60} subunits (Figure 2j). X-ray photoelectron spectroscopy (XPS) revealed a sp^2/sp^3 carbon ratio of 52:8 (Figures 2k and S9), in agreement with the theoretical bonding configuration in qHP-C_{60}, where 52 sp^2 carbons originate from the C_{60} cage and 8 sp^3 carbons arise from intermolecular cross-linking.[2,29]

Sodium-Ion Storage in qHP-C_{60}

Our convective chemical vapor transport method enabled the scalable synthesis of more than 10 g of qHP-C_{60} (Figure 3a), allowing for the fabrication of a 0.8 × 0.1 m^2 electrode on aluminum (Al) foil for battery production (Figures 3b-c and S10). We evaluated the Na-ion storage behavior in a Na||qHP-C_{60} cell using a common organic electrolyte of 1 M sodium perchlorate in ethylene carbonate and propylene carbonate (1:1 by volume) with 5 wt % fluoroethylene carbonate (see Experimental Section). At a current density of 25 mA g^{-1}, qHP-C_{60} delivered a reversible capacity of 279.2 mAh g^{-1} (Figure 3d), far exceeding that of graphite (16.5 mAh g^{-1}) and C_{60} (0.3 mAh g^{-1}). At an elevated current density of 1,000 mA g^{-1}, it maintained a discharge capacity of 147.5 mAh g^{-1}, whereas both graphite and C_{60} exhibited negligible discharge capacities under the same conditions (Figure 3e−f).

To gain deeper insight into the electrochemical kinetics of qHP-C_{60}, we performed cyclic voltammetry measurements at increasing scan rates from 0.3 to 3 mV s^{-1} (Figure S11a). The resulting *b*-values for the anodic and cathodic peaks were 0.604 and 0.551, respectively (Figure S11b), indicating that charge storage was governed by a mixed diffusion-capacitive process in which ion diffusion plays a dominant role.[30] This diffusion-controlled behavior was also supported by the large interlayer spacing of 9.6 Å, which offers low-barrier pathways for Na^+ diffusion. We further confirmed the high cycling stability of qHP-C_{60}, which retained 81.82% of its initial capacity after 300 cycles with an average Coulombic efficiency (CE) of 99.52% (Figure 3g). Even at an elevated current density of 2 A g^{-1}, the

https://doi.org/10.1021/acsnano.6c09620
ACS Nano XXXX, XXX, XXX−XXX

electrode preserved 80% of its capacity after 150 cycles (Figure S12). In addition, the SEM images revealed that the qHP-C_{60} maintained its layered morphology after 300 cycles (Figure S13), confirming the structural robustness during repeated Na-ion insertion and extraction. The relatively low initial CE could be attributed to facilitated electrolyte decomposition for the formation of a solid-electrolyte interphase layer during the initial cycle, due to the presence of edge active sites in qHP-C_{60}.[12]

We performed *in situ* Raman spectroscopy to monitor the evolution of characteristic modes of qHP-C_{60} at 1,420 cm^{-1} and 1,550 cm^{-1} during electrochemical cycling. The intensity of these modes weakened during charging, corresponding to Na^+ deintercalation, and recovered during discharging due to Na^+ intercalation (Figure 3h), indicating the strong Na^+ affinity of qHP-C_{60}. To analyze the potential Na^+ storage sites, we performed density functional theory (DFT) calculations (Figure 3i). The triangular region formed between three adjacent C_{60} subunits (denoted as the "T" region) was identified as an energetically favorable interaction site, originating from the covalently bonded framework, which creates a thermodynamically metastable state. Such a configuration yields an intrinsic driving force to stabilize the inserted Na^+, lowering the energy barrier that normally prevents Na^+ storage in graphite lattices or pristine C_{60} cages.[31,32] This mechanism represents a unique Na-ion storage pathway governed by molecular-scale metastability. Further confirmation of the facilitated Na-ion transport on the qHP-C_{60} surface comes from its reduced diffusion barrier of 0.237 eV, which is significantly lower than that of bare C_{60} molecules (Figure S14). Moreover, the large interlayer spacing of 9.60 Å in qHP-C_{60} further facilitates rapid transport of Na ions, which collectively contributes to the excellent rate performance in Na-ion storage.

Catalytic Properties of qHP-C_{60}

The uneven electron distribution inherent to qHP-C_{60} offers electrocatalytic capability, especially in mediating reversible chloride redox chemistry. In a conversion-type Na−Cl_2 battery, 5 wt % qHP-C_{60} was incorporated with graphite, denoted as the qHP-C_{60} cathode (Figures 4a and S15). For comparison, 5 wt % C_{60} incorporated in graphite (denoted as the C_{60} cathode) and bare graphite cathodes were also prepared. The qHP-C_{60} cathode significantly promoted the reaction kinetics of NaCl/Cl_2 conversion, enabling an ultrahigh current density of 15,000 mA g^{-1} while delivering a reversible capacity of 325 mAh g^{-1}, in contrast to negligible capacities observed with bare graphite and C_{60} cathodes under identical conditions (Figure S16). The Coulombic efficiency for the qHP-C_{60} cathode decreases to ~80% at 15,000 mA g^{-1}. The lower CEs at 15,000 mA g^{-1} can be explained by the decomposition of $SOCl_2$-based electrolyte at high currents, which generates byproducts such as SO_2Cl_2 and S−Cl compounds, giving rise to reduced electrochemical reversibility and lower CEs.[33] Galvanostatic charge−discharge profiles further showed a reduced overpotential of 1.15 V stemming from the qHP-C_{60} cathode, compared to 1.39 V for the C_{60} cathode and 1.21 V for the bare graphite cathode at 1,000 mA g^{-1} (Figure 4b). When benchmarked with state-of-the-art cathode catalysts, including metal−organic and covalent-organic frameworks,[34,35] porous organic nanocages,[36] reduced graphene oxide,[37] and heteroatom-doped carbons,[38] the purely carbonaceous qHP-C_{60} demonstrates outstanding advantages in both catalyst loading (5 wt % versus 60−80 wt %) and maximum current density (15,000 mA g^{-1} versus 1,000−1,500 mA g^{-1}) (Figure 4c). Furthermore, the excellent catalytic capability enabled a maximum NaCl utilization rate of 81.4%, significantly outperforming the range of 16.0−62.5% in previous reports (Figure S17).[33,37,39−41] Even at −20 °C, the Na−Cl_2 battery based on the qHP-C_{60} cathode exhibited stable cycling performance for more than 470 cycles with a charge capacity of 500 mAh g^{-1} (Figure S18).

The impressive electrochemical performance originates from the abundant catalytic edge sites of qHP-C_{60}, which serve as preferential nucleation centers for NaCl deposition during the discharge process (Figures 4d and S19). DFT calculations further confirmed that these edge sites exhibited stronger adsorption energy for $AlCl_4$−NaCl clusters (−3.17 eV) than the basal plane regions (−2.93 eV) (Figures 4e and S20), enabling efficient NaCl/Cl_2 conversion while suppressing electrolyte decomposition. As a result, the qHP-C_{60} cathode afforded a long cycle life exceeding 340 cycles, far outperforming bare graphite (167 cycles) and C_{60} (113 cycles) (Figure S21). This performance ranks among the best cycle lives reported for Na−Cl_2 batteries (Figure S22).[33,37,39−41] Postcycling morphological analysis further confirmed the structural robustness of qHP-C_{60} after 300 cycles (Figures S23a,b and S24a). In stark contrast, pristine C_{60}, which relies solely on weak van der Waals interactions, underwent rapid structural degradation within only 35 cycles (Figures S23c,d and S24b). These results validate the critical role of a covalently bonded architecture in maintaining mechanical and electrochemical stability under extended cycling conditions.[42,43]

Mechanistic studies using *in situ* Raman spectroscopy revealed strong electronic interactions between the $AlCl_4^-$ anion (Al−Cl symmetric stretching at 350 cm^{-1}) and qHP-C_{60} (A_g^2 mode at 1,420 cm^{-1} and H_g^8 mode at 1,550 cm^{-1}) (Figure 4f).[44,45] During charging, the Raman peaks of qHP-C_{60} weakened owing to $AlCl_4^-$ anion adsorption, which perturbs the vibrational modes of the C_{60} subunits. Upon discharge, the peaks recovered as the $AlCl_4^-$ anions desorbed back into the electrolyte. In contrast, graphite exhibited negligible spectral changes (Figure S25), indicating much weaker interactions with $AlCl_4^-$. DFT calculation results further showed a stronger $AlCl_4^-$ adsorption energy on qHP-C_{60} (−3.17 eV) relative to conventional graphite (−2.43 eV), reducing the NaCl* oxidation barrier from 1.48 eV (graphite) to 1.14 eV (qHP-C_{60}) (Figures 4g and S26). Differential charge density and Bader charge analyses revealed an accelerated electron transfer pathway between qHP-C_{60} and NaCl, via the formation of a "qHP-C_{60}−$AlCl_3$−$NaCl_2$*" complex, which facilitates NaCl oxidation and improves interfacial reaction kinetics along the electroactive edges (Figure 4h). Electrochemical impedance spectroscopy (EIS) measurements further revealed a lower charge-transfer resistance (R_{ct}) of 37.1 Ω for qHP-C_{60}, versus 73.0 Ω for bare graphite (Figure S27), confirming that qHP-C_{60} facilitates more efficient interfacial charge transfer.

Overall, this study advances the field by establishing qHP-C_{60} as a topology-engineered multifunctional carbon material that integrates high-capacity Na-ion storage and intrinsic catalytic activity within a single all-carbon covalent framework. Especially, the covalent intermolecular bridge bonds create abundant accessible sites for Na^+ adsorption, enabling a high reversible Na-ion storage capacity of up to 279 mAh g^{-1} at 25

https://doi.org/10.1021/acsnano.6c09620
ACS Nano XXXX, XXX, XXX−XXX

mA g^{-1}. Furthermore, edge-localized charge redistribution markedly promotes the catalytic kinetics of $NaCl/Cl_2$ conversion, delivering a record rate capability of 15,000 mA g^{-1} with a substantially reduced catalyst loading of only 5 wt %, compared with the typical 60−80 wt % required for benchmark catalysts. Despite these promising results, several challenges should still be addressed to enable practical battery applications of qHP-C_{60}. Although gram-scale synthesis of qHP-C_{60} and large-area electrode fabrication have already been demonstrated, further efforts are needed to reduce the material cost, particularly in comparison with other low-cost carbon-based materials. From an electrochemical perspective, optimization of the molecular structure of qHP-C_{60} is required to effectively expose and utilize the internal catalytic sites, thereby enhancing its catalytic performance and broadening its applicability to other conversion-type battery systems. In addition, rational engineering of the electrolyte-electrode interface will be crucial for further improving the long-term stability of qHP-C_{60} when applied to reactive electrolytes.

CONCLUSION

In summary, we report sodium storage and electrocatalytic conversion properties in layered fullerene networks. The quasi-hexagonal covalent framework not only enhances structural stability but also introduces emergent electronic and catalytic properties that enable efficient Na-ion storage and chlorine redox chemistry, achieving excellent electrochemical performance in both Na-ion batteries and conversion-type Na−Cl_2 batteries. The formation of intermolecular bridging bonds generates a high density of electroactive sites that thermodynamically stabilize intercalated Na^+ ions, while the large interlayer spacing of 9.60 Å kinetically facilitates rapid Na-ion transport. In addition, the electron density redistribution at the edges of qHP-C_{60}, induced by intermolecular covalent bonding, significantly enhances catalytic activity for $NaCl/Cl_2$ redox reactions, making it one of the most promising cathode catalysts reported for Na−Cl_2 batteries. The combination of *ab initio* structural design and topological control establishes an attractive platform for engineering functional carbon materials, opening an avenue for efficient energy storage.

EXPERIMENTAL SECTION

Materials: C_{60} powder (99.9%) was purchased from Suzhou Dade Carbon Nano Technology Co., Ltd. Mg nuggets (99.0%), salicylic acid (99.5%), *N*-methylpyrrolidone (NMP, 99.5%), and ethanol (99.5%) were acquired from Sinopharm Chemical Reagent Co., Ltd. Thionyl chloride ($SOCl_2$, 99.0%) was received from Energy Chemical (Shanghai). Aluminum chloride ($AlCl_3$, 99.0%) was purchased from TCI Development Co., Ltd. Sodium bis(fluorosulfonyl)imide (NaFSI, 99.9%) and sodium bis(trifluoromethylsulfonyl)imide (NaTFSI, 99.9%) were sourced from Changde Dado New Material Co., Ltd. Sodium metal cubes (Na, 99.7%) were acquired from Shanghai Aladdin Biochemical Technology Co., Ltd. Nickel foam (Ni, 0.5 mm thick), Ketjenblack (KJ, ECP-600JD), and polytetrafluoroethylene emulsion binder (PTFE, 60 wt % aqueous dispersion, Daikin, D-210C) were purchased from Cyber Electrochemical Materials. The commercial ester-based electrolyte composed of 1 M sodium perchlorate ($NaClO_4$) in a mixture solvent of ethylene carbonate (EC) and propylene carbonate (PC) (1:1 by volume), containing 5 wt % fluoroethylene carbonate (FEC), was purchased from Duoduo Reagent. NaFSI and NaTFSI were dried in a vacuum oven at 90 °C overnight prior to use. All the other chemicals were used as received without further purification.

Preparation of Mg_4C_{60} and qHP-C_{60}:Mg_4C_{60} crystals were prepared by a convective chemical vapor transport approach, with Mg nuggets serving as the Mg source. 75 mg of Mg and 150 mg of C_{60} powder were placed into two terminals of a quartz tube, spaced 35 cm apart. The tube was then evacuated and transferred into a multizone tubular furnace with a temperature gradient of 500−600 °C for 40 h. Micrometer-scale Mg_4C_{60} crystals formed in the region with a temperature of 500 °C. The Mg_4C_{60} crystals were used as precursors to synthesize qHP-C_{60} through a combined acid etching and chelate-driven Mg removal process. To prepare the etching solution, 200 mL of 2 M nitric acid (HNO_3) aqueous solution and 200 mL of 2 M salicylic acid in *N*-methylpyrrolidone were mixed thoroughly under constant stirring at room temperature. One gram of Mg_4C_{60} crystals was then added to the solution and allowed to react for 24 h at room temperature. After the reaction, the resulting qHP-C_{60} was washed three times with N,N-dimethylformamide and ethanol, and dried at 80 °C in a vacuum oven, yielding approximately 0.88 g of the final product.

Preparation of electrolytes and electrodes: All electrolytes were prepared in an argon-filled glovebox with the contents of H_2O and O_2 below 1 ppm. The $SOCl_2$-based electrolyte was prepared by dissolving 4 M $AlCl_3$ in $SOCl_2$, followed by adding 2 wt % NaFSI and 2 wt % NaTFSI (relative to the total weight of $AlCl_3$ and $SOCl_2$). The mixture was stirred at 800 rpm for 4 h to prepare the electrolyte. For Na−Cl_2 batteries, the cathode slurry was made by mixing graphite, qHP-C_{60}, and PTFE in ethanol at a weight ratio of 85:5:10. The mixture was sonicated until the carbon materials were uniformly dispersed. Ni foams with a diameter of 14 mm were cut using a manual disk cutter (MTI, MSK-T-10) and cleaned by ultrasonic treatment in ethanol for 10 min. The obtained cathode slurry was applied dropwise (80 μL each time) onto a Ni foam hovered over a 100 °C hot plate. After each drop, a 5-min rest ensured complete ethanol evaporation. This process was repeated until the carbon mass loading reached 2−3 mg cm^{-2}. The resulting carbon cathodes were dried overnight in a vacuum oven at 100 °C and then roll-pressed into thin electrodes. For comparison, graphite and C_{60} cathodes were prepared using the same method, with slurry compositions adjusted to graphite:PTFE = 90:10 and graphite:C_{60}:PTFE = 85:5:10, respectively. For Na-ion batteries, electrodes were prepared by mixing qHP-C_{60}, super P, and PVDF in NMP with a weight ratio of 80:10:10, followed by grinding in an agate mortar for 2 h at 25 °C. The slurry was then coated onto a carbon-coated Al foil and dried under vacuum at 100 °C for 24 h, which was further rolled to form the qHP-C_{60} electrode.

Preparation and characterization of batteries: All batteries were assembled in an argon-filled glovebox with the contents of H_2O and O_2 below 1 ppm. The Na metal anodes were prepared by removing the surface oxide layer from a rinsed Na metal cube using a clean blade, followed by pressing the Na metal into a thin foil (14 mm in diameter). The Na−Cl_2 batteries were fabricated in 2032-type coin cells (grade 316 stainless steel), using glass fiber separators (GF/D, Whatman, 16 mm in diameter). A cathode (14 mm in diameter) and Na foil were separated by two glass fiber separators with 150 μL of electrolyte. For Na-ion batteries, a qHP-C_{60} electrode (12 mm in diameter) and Na foil were separated by one glass fiber separator with 120 μL of electrolyte. All coin cells were hermetically sealed using a digital pressure-controllable electric crimper (MTI, MSK-160E). Galvanostatic charge−discharge measurements were conducted on a Neware battery testing system (CT-4008Tn-5 V6A-S1).

Material Characterization: Morphological characterization was carried out using a field-emission scanning electron microscope (ZEISS Gemini SEM 300) at an accelerating voltage of 5 kV. Crystalline phases were identified by X-ray diffraction using a Thermo Scientific ARL Equinox 3500 diffractometer with Cu Kα radiation (λ = 0.154 nm). Raman spectroscopy was conducted using a LabRAM Soleil confocal system with a 532 nm excitation laser. In situ Raman measurements were performed using a spectroelectrochemical cell (MicroElab), with a spectrum recorded every 5 min. High-resolution transmission electron microscopy was performed with a Thermo Fisher TALOS F200X instrument operated at 200 kV. Surface chemical composition was analyzed by X-ray photoelectron spectroscopy using monochromatic Al Kα X-rays (1,486.6 eV) on a Thermo

https://doi.org/10.1021/acsnano.6c09620
ACS Nano XXXX, XXX, XXX−XXX

Scientific ESCALAB Xi system, with all binding energies calibrated to the C 1s peak (284.8 eV). Solid-state ^{13}C NMR was conducted on a Bruker AVANCE NEO 600 WB spectrometer.

Computational details: All density functional theory (DFT) calculations were performed using the Vienna Ab Initio Simulation Package (VASP).[46,47] The generalized gradient approximation method with the Perdew–Burke–Ernzerhof (PBE) exchange-correlation function was used to manage the electron exchange and correlation energy.[48] The plane wave basis (kinetic energy cutoff value: 450 eV) was used to describe the valence electrons. All calculations were performed using the k-point sampling obtained from the gamma center with a 1 × 1 × 1 mesh. The atomic positions were fully optimized until the energy and forces converged to 1×10^{-5} eV and 0.03 eV $Å^{-1}$, respectively. The Na-ion diffusion barriers were evaluated using the climbing-image nudged elastic band (CI-NEB) method, which identifies the minimum-energy migration pathway and the corresponding transition state between two stable adsorption sites. The Na adsorption energy (E_{ads}) was considered as follows:

$$E_{ads} = E_{*X} - E_{*} - E_{X}$$

where E_{*X}, E_{*}, E_X is the total energy of the intermediates adsorbed on the system, the system, and the intermediates, respectively.

The charge difference was obtained as follows:

$$\rho = \rho_{AB} - \rho_B - \rho_A$$

where ρ_{AB}, ρ_A, and ρ_B is the charge density of $AlCl_3$–$NaCl_2$ adsorbed at C_{60} or C, C_{60}, or C, and $AlCl_3$–$NaCl_2$, respectively.

Vapor pressure calculations: The vapor pressure of Mg was estimated based on the literature data.[49] For C_{60}, the vapor pressure was calculated by the Clausius–Clapeyron equation:[50]

$$\ln P = -\frac{\Delta H_m}{RT} + C$$

where P, ΔH_m, R, T, and C represent the vapor pressure, molar enthalpy of evaporation, molar gas constant 8.314 J $(mol·K)^{-1}$, temperature, and a constant, respectively. The ΔH_m of C_{60} was 183.5 kJ mol^{-1}.

■ ASSOCIATED CONTENT

Supporting Information

The Supporting Information is available free of charge at https://pubs.acs.org/doi/10.1021/acsnano.6c09620.

The synthesis of Mg_4C_{60} crystals and layered C_{60} networks; additional morphological and structural analysis of the samples; and electrochemical analysis of the prepared batteries, including *in situ* and *ex-situ* measurements, cycling, and rate performances (DOCX)

■ AUTHOR INFORMATION

Corresponding Authors

Hao Sun – *Frontiers Science Center for Transformative Molecules, School of Chemistry and Chemical Engineering, Zhangjiang Institute for Advanced Study, Shanghai Jiao Tong University, Shanghai 200240, China;* orcid.org/0000-0003-4599-5518; Email: haosun@sjtu.edu.cn

Paolo Samorì – *University of Strasbourg & CNRS, ISIS & icFRC, Strasbourg 67000, France;* orcid.org/0000-0001-6256-8281; Email: samori@unistra.fr

Sheng Yang – *Frontiers Science Center for Transformative Molecules, School of Chemistry and Chemical Engineering, Zhangjiang Institute for Advanced Study, Shanghai Jiao Tong University, Shanghai 200240, China*; Email: sheng.yang@sjtu.edu.cn

Authors

Hao Mei – *Frontiers Science Center for Transformative Molecules, School of Chemistry and Chemical Engineering, Zhangjiang Institute for Advanced Study, Shanghai Jiao Tong University, Shanghai 200240, China*

Qiuchen Xu – *Frontiers Science Center for Transformative Molecules, School of Chemistry and Chemical Engineering, Zhangjiang Institute for Advanced Study, Shanghai Jiao Tong University, Shanghai 200240, China*

Shitao Wu – *Shanghai Key Laboratory of High-Resolution Electron Microscopy, Shanghai Tech University, Shanghai 201210, China;* orcid.org/0000-0002-2737-6011

Yan Wang – *Frontiers Science Center for Transformative Molecules, School of Chemistry and Chemical Engineering, Zhangjiang Institute for Advanced Study, Shanghai Jiao Tong University, Shanghai 200240, China*

Wentao Fan – *Frontiers Science Center for Transformative Molecules, School of Chemistry and Chemical Engineering, Zhangjiang Institute for Advanced Study, Shanghai Jiao Tong University, Shanghai 200240, China*

Yuxuan Zhang – *Frontiers Science Center for Transformative Molecules, School of Chemistry and Chemical Engineering, Zhangjiang Institute for Advanced Study, Shanghai Jiao Tong University, Shanghai 200240, China*

Shuo Wang – *Frontiers Science Center for Transformative Molecules, School of Chemistry and Chemical Engineering, Zhangjiang Institute for Advanced Study, Shanghai Jiao Tong University, Shanghai 200240, China*

Hui Yu – *Frontiers Science Center for Transformative Molecules, School of Chemistry and Chemical Engineering, Zhangjiang Institute for Advanced Study, Shanghai Jiao Tong University, Shanghai 200240, China*

Shitao Geng – *Frontiers Science Center for Transformative Molecules, School of Chemistry and Chemical Engineering, Zhangjiang Institute for Advanced Study, Shanghai Jiao Tong University, Shanghai 200240, China*

Chengxiao Zhang – *Frontiers Science Center for Transformative Molecules, School of Chemistry and Chemical Engineering, Zhangjiang Institute for Advanced Study, Shanghai Jiao Tong University, Shanghai 200240, China*

Shanshan Tang – *Frontiers Science Center for Transformative Molecules, School of Chemistry and Chemical Engineering, Zhangjiang Institute for Advanced Study, Shanghai Jiao Tong University, Shanghai 200240, China*

Antonio Gaetano Ricciardulli – *University of Strasbourg & CNRS, ISIS & icFRC, Strasbourg 67000, France;* orcid.org/0000-0003-2688-9912

Yiyong Mai – *Frontiers Science Center for Transformative Molecules, School of Chemistry and Chemical Engineering, Zhangjiang Institute for Advanced Study, Shanghai Jiao Tong University, Shanghai 200240, China;* orcid.org/0000-0002-6373-2597

Huisheng Peng – *State Key Laboratory of Molecular Engineering of Polymers, Department of Macromolecular Science, and Institute of Fiber Materials and Devices, Fudan University, Shanghai 200438, China;* orcid.org/0000-0002-2142-2945

Complete contact information is available at: https://pubs.acs.org/10.1021/acsnano.6c09620

Author Contributions

[⊥]H.M. and Q.X. contributed equally to this work. S.Y., P.S., and H.S. conceived and designed the project. H.M. prepared carbon materials and conducted characterizations. Q.X. fabricated rechargeable Na−Cl_2 and Na-ion batteries and performed electrochemical characterizations. S.W. and Y.Z. performed morphology characterization. Y. W. fabricated large-scale electrodes. W.F. and H.Y. performed in situ Raman tests. S.W., S.G., and C.Z. conducted in situ XRD tests. S.T. performed the density functional theory simulations. A.G.R., H.P., Y.M., and P.S. provided suggestions for this study. All the authors discussed and analyzed the data. H.M., Q.X., H.S., and S.Y. wrote the manuscript.

Notes

The authors declare no competing financial interest.

■ ACKNOWLEDGMENTS

The authors gratefully acknowledge the financial support from the National Natural Science Foundation of China (grant nos. 22205141 and 22575145), the Scientific Research Innovation Capability Support Project for Young Faculty (SRICSPYF-ZY2025049), the Science and Technology Commission of Shanghai Municipality (grant no. 24CL2900100), the Shanghai Municipal Science and Technology Major Project, the Fundamental Research Funds for the Central Universities of China (grant no. 26X010301678 and 26X010301599), the Autonomous Project of the State Key Laboratory of Synergistic Chem-Bio Synthesis (grant no. sklscbs202557), the LUI Che Woo Talent Development Fund (LCW-ZIAS-2026B05), the SJTU 2030B plan (No. WH510207202), and the European Commission through the HORIZON-CL4-2023-DIGITAL-EMERGING-01-CNECT project 2D-PRINTABLE (GA-101135196), the Agence Nationale de la Recherche through the Interdisciplinary Thematic Institute SysChem via the IdEx Unistra (ANR-10-IDEX-0002) within the program Investissement d'Avenir, the Foundation Jean-Marie Lehn, the Institut Universitaire de France (IUF). The authors sincerely acknowledge Yulong Men from the Central Analytical Lab, School of Chemistry and Chemical Engineering, Shanghai Jiao Tong University, for his assistance with the XPS tests.

■ REFERENCES

(1) Zhao, S.; Huang, F. Weakly Solvating Few-Layer-Carbon Interface toward High Initial Coulombic Efficiency and Cyclability Hard Carbon Anodes. *ACS Nano* **2024**, *18* (2), 1733−1743.
(2) Hou, L.; Cui, X.; Guan, B.; Wang, S.; Li, R.; Liu, Y.; Zhu, D.; Zheng, J. Synthesis of a Monolayer fullerene network. *Nature* **2022**, *606*, 507−510.
(3) Meirzadeh, E.; Evans, A. M.; Rezaee, M.; Milich, M.; Dionne, C. J.; Darlington, T. P.; Bao, S. T.; Bartholomew, A. K.; Handa, T.; Rizzo, D. J.; Wiscons, R. A.; Reza, M.; Zangiabadi, A.; Fardian-Melamed, N.; Crowther, A. C.; Schuck, P. J.; Basov, D. N.; Zhu, X.; Giri, A.; Hopkins, P. E.; Kim, P.; Steigerwald, M. L.; Yang, J.; Nuckolls, C.; Roy, X. A few-layer covalent network of fullerenes. *Nature* **2023**, *613*, 71−76.
(4) Park, J.; Cho, S.; Shin, S.; Kim, R.; Shin, D.; Shin, Y. Overview of graphite supply chain and its challenges. *Geosci J* **2025**, *29* (3), 329−341.
(5) Zhao, L.; Ding, B.; Qin, X. Y.; Wang, Z.; Lv, W.; He, Y. B.; Yang, Q. H.; Kang, F. Revisiting the roles of natural graphite in ongoing lithium-ion batteries. *Adv. Mater* **2022**, *34* (18), 2106704.
(6) Li, Y.; Lu, Y.; Adelhelm, P.; Titirici, M. M.; Hu, Y. S. Intercalation chemistry of graphite: alkali metal ions and beyond. *Chem. Soc. Rev* **2019**, *48* (17), 4655−4687.
(7) Yuan, B.; Xu, Q.; Zhao, X.; Geng, S.; Tang, S.; Zhang, C.; Sun, H. Revitalizing Chlorine−Based Batteries for Low−Cost and High−Performance Energy Storage. *Adv. Energy Mater* **2024**, *14* (5), 2303127.
(8) Yao, W.; Liao, K.; Lai, T.; Sul, H.; Manthiram, A. Rechargeable metal-sulfur batteries: key materials to mechanisms. *Chem. Rev* **2024**, *124* (8), 4935−5118.
(9) Tu, S.; Zhang, B.; Zhang, Y.; Chen, Z.; Wang, X.; Zhan, R.; Ou, Y.; Wang, W.; Liu, X.; Duan, X.; Wang, L.; Sun, Y. Fast-charging capability of graphite-based lithium-ion batteries enabled by Li_3P-based crystalline solid−electrolyte interphase. *Nat. Energy* **2023**, *8* (12), 1365−1374.
(10) Zhang, Y.; Zhang, S.; Chu, Y.; Zhang, J.; Xue, H.; Jia, Y.; Cao, T.; Qiu, D.; Zou, X.; Wang, D.; et al. Redefining closed pores in carbons by solvation structures for enhanced sodium storage. *Nat. Commun* **2025**, *16* (1), 3634.
(11) Li, Y.; Vasileiadis, A.; Zhou, Q.; Lu, Y.; Meng, Q.; Li, Y.; Ombrini, P.; Zhao, J.; Chen, Z.; Niu, Y.; Qi, X.; Xie, F.; van der Jagt, R.; Ganapathy, S.; Titirici, M.; Li, H.; Chen, L.; Wagemaker, M.; Hu, Y. Origin of fast charging in hard carbon anodes. *Nat. Energy* **2024**, *9* (2), 134−142.
(12) Lu, Z.; Yang, H.; Guo, Y.; Lin, H.; Shan, P.; Wu, S.; He, P.; Yang, Y.; Yang, Q.; Zhou, H. Consummating ion desolvation in hard carbon anodes for reversible sodium storage. *Nat. Commun* **2024**, *15* (1), 3497.
(13) Zhu, H.; Peng, L.; Wu, J.; Li, S.; Wu, Q.; Cheng, S.; Xie, J.; Lu, J. Fluorine-doped micropore-covered mesoporous carbon nanofibers for long-lasting anode-free sodium metal batteries. *Nat. Commun* **2025**, *16* (1), 5494.
(14) Huang, P.; Li, Z.; Chen, L.; Li, Y.; Liu, Z.; Zhang, J.; Luo, J.; Zhang, W.; Liu, W.; Zhang, X.; Zhu, R.; Chen, Y. Ultrafast dual-shock chemistry synthesis of ordered/disordered hybrid carbon anodes: high-rate performance of Li-ion batteries. *ACS Nano* **2024**, *18* (28), 18344−18354.
(15) Usiskin, R.; Lu, Y.; Popovic, J.; Law, M.; Balaya, P.; Hu, Y.; Maier, J. Fundamentals, status and promise of sodium-based batteries. *Nat. Rev. Mater* **2021**, *6* (11), 1020−1035.
(16) Pei, B.; Yu, H.; Zhang, L.; Fang, G.; Zhou, J.; Cao, X.; Liang, S. Hard carbon for sodium-ion batteries: from fundamental research to practical applications. *Adv. Mater* **2025**, *37* (39), 2504574.
(17) Li, Z.; Liu, Q.; Wang, X. Two-dimensional cluster-assembled materials with properties beyond their individualities and bulks. *Matter* **2023**, *6* (11), 3747−3762.
(18) Bao, L.; Xu, T.; Guo, K.; Huang, W.; Lu, X. Supramolecular engineering of crystalline fullerene micro-/nano-architectures. *Adv. Mater* **2022**, *34* (52), 2200189.
(19) Chang, X.; Xu, Y.; von Delius, M. Recent advances in supramolecular fullerene chemistry. *Chem. Soc. Rev* **2024**, *53* (1), 47−83.
(20) Baskar, A. V.; Benzigar, M. R.; Talapaneni, S. N.; Singh, G.; Karakoti, A. S.; Yi, J.; Al Muhtaseb, A. H.; Ariga, K.; Ajayan, P. M.; Vinu, A. Self-assembled fullerene nanostructures: synthesis and applications. *Adv. Funct. Mater* **2022**, *32* (6), 2106924.
(21) Pan, F.; Ni, K.; Xu, T.; Chen, H.; Wang, Y.; Gong, K.; Liu, C.; Li, X.; Lin, M.; Li, S.; Wang, X.; Yan, W.; Yin, W.; Tan, P.; Sun, L.; Yu, D.; Ruoff, R. S.; Zhu, Y. Long-range ordered porous carbons produced from C_{60}. *Nature* **2023**, *614*, 95−101.
(22) Zhang, S.; Li, Z.; Luo, K.; He, J.; Gao, Y.; Soldatov, A. V.; Benavides, V.; Shi, K.; Nie, A.; Zhang, B.; et al. Discovery of carbon-based strongest and hardest amorphous material. *Natl. Sci. Rev* **2022**, *9*, nwab140.
(23) Huang, C.; Wang, T.; Wang, X.; Chen, M.; Yang, S.; Du, P. Monolayer covalent C_{60} networks anchored with uniform ultrasmall iridium nanoparticles for boosting electrocatalytic hydrogen evolution. *ACS Nano* **2025**, *19* (19), 18620−18629.
(24) Ricco, M.; Shiroka, T.; Belli, M.; Pontiroli, D.; Pagliari, M.; Ruani, G.; Palles, D.; Margadonna, S.; Tomaselli, M. Unusual polymerization in the Li_4C_{60} fulleride. *Phys. Rev. B* **2005**, *72* (15), 155437.

https://doi.org/10.1021/acsnano.6c09620
ACS Nano XXXX, XXX, XXX−XXX

(25) Bormann, D.; Sauvajol, J. L.; Goze, C.; Rachdi, F.; Moreac, A.; Girard, A.; Forro, L.; Chauvet, O. Raman study of the polymerized state of RbC_{60} and CsC_{60}. *Phys. Rev. B* **1996**, *54* (19), 14139−14145.
(26) Wagberg, T.; Sundqvist, B. Raman study of the two-dimensional polymers Na_4C_{60} and tetragonal C_{60}. *Phys. Rev. B* **2002**, *65* (15), 155421.
(27) Wang, X.; Chen, X.; Lv, R.; Ma, H.; Yao, Y.; Jin, H.; Qiao, S.; Sun, Y.; Liu, D.; Song, L.; et al. Modulating the binding strength of multiple intermediates by few-layer fullerene network electron buffer for alkaline hydrogen evolution. *Small* **2025**, *21* (32), 2506131.
(28) Rachdi, F.; Goze, C.; Hajji, L.; Thier, K. F.; Zimmer, G.; Mehring, M.; Nunez-Regueiro, M. High resolution NMR studies of one and two dimensional polymerized C_{60}: Polymeric fullerenes. *Appl. Phys. A: Mater. Sci. Process* **1997**, *64* (3), 295−299.
(29) Zhao, X.; Zhang, Y.; Zhao, J.; Hu, H.; Li, J. Understanding the electronic structure and chemical bonding in the 2D fullerene monolayer. *Inorg. Chem* **2024**, *63* (25), 11572−11582.
(30) Zhang, X.; Huang, Y.; Li, X.; Yan, F.; Chen, Z.; Zhang, Z.; Lv, Z.; Liu, L.; Li, Q.; Li, W.; et al. Regulating Local Mn—O Coordination to Suppress the Intrinsic Anti-Site Defects in Mn-Based Phosphate Cathodes. *Adv. Energy Mater* **2025**, No. e05250.
(31) Choudhary, S.; Saroha, R.; Banerjee, S. Efficient electron injection into graphullerene enables reversible NaC_2 sodium storage. *ACS Appl. Mater. Interfaces* **2024**, *16* (38), 50859−50869.
(32) Yao, A.; Benson, S. M.; Chueh, W. C. Critically assessing sodium-ion technology roadmaps and scenarios for techno-economic competitiveness against lithium-ion batteries. *Nat. Energy* **2025**, *10* (3), 404−416.
(33) Zhu, G.; Tian, X.; Tai, H.; Li, Y.; Li, J.; Sun, H.; Liang, P.; Angell, M.; Huang, C.; Ku, C.; Hung, W.; Jiang, S.; Meng, Y.; Chen, H.; Lin, M.; Hwang, B.; Dai, H. Rechargeable Na/Cl_2 and Li/Cl_2 batteries. *Nature* **2021**, *596*, 525−530.
(34) Xu, Y.; Jiao, L.; Ma, J.; Zhang, P.; Tang, Y.; Liu, L.; Liu, Y.; Ding, H.; Sun, J.; Wang, M.; Li, Z.; Jiang, H.; Chen, W. Metal-organic frameworks for nanoconfinement of chlorine in rechargeable lithium-chlorine batteries. *Joule* **2023**, *7* (3), 515−528.
(35) Xu, Y.; Wang, M.; Sajid, M.; Meng, Y.; Xie, Z.; Sun, L.; Jin, J.; Chen, W.; Zhang, S. Organocatalytic lithium chloride oxidation by covalent organic frameworks for rechargeable lithium-chlorine batteries. *Angew. Chem., Int. Ed* **2024**, *63* (7), No. e202315931.
(36) Xu, Y.; Zhang, S.; Wang, M.; Meng, Y.; Xie, Z.; Sun, L.; Huang, C.; Chen, W. Enrichment of Chlorine in Porous Organic Nanocages for High-Performance Rechargeable Lithium-Chlorine Batteries. *J. Am. Chem. Soc* **2023**, *145* (50), 27877−27885.
(37) Feng, W.; Wei, X.; Yang, J.; Ma, C.; Sun, Y.; Han, J.; Kong, D.; Zhi, L. Iodine-induced self-depassivation strategy to improve reversible kinetics in $Na-Cl_2$ battery. *Nat. Commun* **2024**, *15* (1), 6904−6912.
(38) Wei, X.; Kong, D.; Feng, W.; Cao, F.; Ma, C.; Yang, J.; Han, J.; Wang, L.; Ma, G.; Wang, H.; et al. Protonated pyridinic nitrogen enhances chloride conversion for ultrastable $Li/Na-Cl_2$ batteries. *Adv. Energy Mater* **2025**, *15* (31), 2501333.
(39) Liang, P.; Zhu, G.; Wang, W.; Huang, C. L.; Wu, S. C.; Zhou, J.; Zhou, X.; Wu, Y.; Wang, S.; Wang, M.; Zhang, L.; Ming, C. C.; Li, J.; Wang, F.; Sun, M.; Li, Y. Y.; Hwang, B. J.; Dai, H. Carbon nanotubes for rechargeable Na/Cl_2 batteries. *J. Am. Chem. Soc* **2025**, *147* (22), 18541−18549.
(40) Xiang, L.; Xu, Q.; Zhang, H.; Geng, S.; Cui, R.; Xiao, T.; Chen, P.; Wu, L.; Yu, W.; Peng, H.; et al. Ultrahigh-rate Na/Cl_2 batteries through improved electron and ion transport by heteroatom-doped bicontinuous-structured carbon. *Angew. Chem., Int. Ed* **2023**, *62* (47), No. e202312001.
(41) Ma, C.; Feng, W.; Kong, D.; Wei, X.; Gong, X.; Yang, J.; Han, J.; Zhi, L. Vertical-channel cathode host enables rapid deposition kinetics toward high-areal-capacity sodium-chlorine batteries. *Small* **2024**, *20* (29), 2310978.
(42) Wang, S.; Liu, H.; Lei, Y.; Li, D.; Fan, Y.; Hong, L.; Guo, X.; Wang, M.; Huang, Z.; Chen, Y.; Yang, X.; Zhang, J.; Li, H.; Wang, G. Covalent Bridges Enabling Layered C_{60} as an Exceptionally Stable Anode in Lithium-Ion Batteries. *J. Am. Chem. Soc* **2025**, *147* (51), 47663−47674.
(43) Huang, C.; Yang, Y.; Li, M.; Qi, X.; Pan, C.; Guo, K.; Bao, L.; Lu, X. Ultrahigh capacity from complexation-enabled aluminum-ion batteries with C_{70} as the cathode. *Adv. Mater* **2024**, *36* (6), No. e2306244.
(44) Mosier-Boss, P. A.; Boss, R. D.; Gabriel, C. J.; Szpak, S.; Smith, J. J.; Nowak, R. J. Raman and infrared spectroscopy of the $AlCl_3-SOCl_2$ system. *J. Chem. Soc., Faraday Trans. 1* **1989**, *85* (1), 11−21.
(45) Hou, Y.; Nie, B.; Li, Z. Raman spectroscopy of $AgNO_3$ complex encapsulated fullerene (C_{60}) microcube. *Vib. Spectrosc* **2020**, *109*, 103089.
(46) Kresse, G.; Hafner, J. Ab Initio Molecular Dynamics for Liquid Metals. *Phys. Rev. B* **1993**, *47*, 558−561.
(47) Kresse, G.; Furthmuller, J. Efficiency of Ab-Initio Total Energy Calculations for Metals and Semiconductors Using a Plane-Wave Basis Set. *Comput. Mater. Sci.* **1996**, *6*, 15−50.
(48) Kresse, G.; Joubert, D. From Ultrasoft Pseudopotentials to the Projector Augmented-Wave Method. *Phys. Rev. B* **1999**, *59*, 1758−1775.
(49) Greenbank, J. C.; Argent, B. B. Vapour Pressure of Magnesium, Zinc and Cadmium. *Trans. Faraday Soc.* **1965**, *61*, 655−664.
(50) Pankajavalli, R; Mallika, C; Sreedharan, O.M; Premila, M; Gopalan, P. Vapour Pressure of C_{60} by a Transpiration Method Using a Horizontal Thermobalance. *Thermochim. Acta* **1998**, *316*, 101−108.

https://doi.org/10.1021/acsnano.6c09620
ACS Nano XXXX, XXX, XXX−XXX